

MID-INFRARED PHOTOMETRY AND SPECTRA OF THREE HIGH MASS PROTOSTARS AT IRAS 18151-1208 AND IRAS 20343+4129

M. F. Campbell^{1,8}, T. K. Sridharan^{2,8}, H. Beuther³, J. H. Lacy⁴, J. L. Hora², M. Kassis⁵, M. Saito⁷, J. M. De Buizer⁷, S. H. Fung¹, and L. C. Johnson¹

ABSTRACT

We present arcsecond-scale mid-ir photometry (in the N band and at $24.8 \mu\text{m}$), and low resolution spectra in the N band ($R \simeq 100$) of a high mass protostellar object (HMPO) in IRAS 18151-1208 and of two HMPOs in IRAS 20343+4129, IRS1 and IRS3. In addition we present high resolution mid-ir spectra ($R \simeq 80000$) of the two HMPOs in IRAS 20343+4129. These data are used with simple models to estimate the amounts gas and dust associated with the mid-ir emitting clumps, the amounts of overlying absorbing dust and gas, the mid-ir luminosities of the HMPOs, and the likely spectral type of the HMPO for which [NeII] $12.8 \mu\text{m}$ emission was detected (IRAS 20343+4129 IRS3).

Subject headings:

¹Department of Physics and Astronomy, Colby College, Waterville, ME 04901

²Center for Astrophysics, 60 Garden Street, Cambridge, MA 02138

³Max-Planck-Institut für Astronomie, Königstuhl 17, Heidelberg, Germany D-69117

⁴University of Texas, Department of Astronomy, Austin, TX 78712

⁵W. H. Keck Observatory, 65-1120 Mamalahoa Highway, Kamuela, HI 96743

⁶(National Astronomical Observatory of Japan, Osawa 2-21-1, Mitaka, Tokyo 181-8588

⁷Gemini Observatory, Casilla, La Serena, Chile

⁸Visiting Astronomer at the Infrared Telescope Facility, which is operated by the University of Hawaii under Cooperative Agreement no. NCC 5-538 with the National Aeronautics and Space Administration, Science Mission Directorate, Planetary Astronomy Program.

1. Introduction

Many open questions in high-mass star formation are related to the evolution of circumstellar envelopes, accretion disks, and jets from high-mass protostellar objects (HMPOs). HMPOs are often bright sources in mid-ir continuum, but only in a few recent cases have images suggested specific structures: De Buizer & Minier (2005) have observed hot dust located on a disk and on the outflow cavity wall surrounding the HMPO NGC7538 IRS,1 and De Buizer (2006) imaged a jet-like structure also believed to be due to dust on the cavity wall in G34.20-0.74. Mid-ir ionic lines like [NeII] and [SIV] have been used to map compact and ultracompact HII regions and photodissociation regions, and to study their structure and excitation (Lacy et al. 1982; Okamoto et al. 2001; Zhu et al. 2005; Kassis et al. 2002, 2006), but there is a lack of observations of HMPOs. A remarkable feature of high-mass star formation is that HMPOs, defined as actively accreting mass, can begin nuclear fusion and hence also be pre-main sequence or main sequence stars that are already ionizing hypercompact or ultracompact HII regions (Beuther et al. 2006). This feature raises a possibility of determining the spectral type of an HMPO through the ionic lines excitation, or from estimating the number of ionizing photons required for its observed centimeter continuum flux, separately from estimating its luminosity from infrared emission, and then deducing its spectral type. However there is also the possibility that the ionization is collisionally excited by a jet. It may be possible to distinguish between the two cases, depending of Doppler velocities and morphology.

Hoping to enlarge the sample of HMPOs that could be studied in detail despite potential limitations, in 2003 we made mid-ir observations on the IRTF of about a third of the survey of 69 HMPOs presented by Sridharan et al. (2002) and Beuther et al. (2002a). We chose objects from their survey that appeared compact in the MSX survey, and found that about 80% of them were unresolved or marginally resolved by MIRSI (Deutsch et al. 2002) on the IRTF in N band and in a narrow band filter at $24.8 \mu\text{m}$. In addition, we obtained MIRSI grism low-resolution spectra ($R \simeq 100$) of ten of them in the N band. In 2006 on Gemini North, we have obtained TEXES (Lacy et al. 2002) high-resolution spectra ($R \simeq 80000$) of two HMPOs for which we had grism spectra. In this paper we present spectra and photometry of three HMPOs including the two with TEXES spectra: IRAS 18151-1208, IRAS 20343+4129 IRS1, and IRAS 20343+4139 IRS3. We will demonstrate that mid-ir emission from the dust and gas near the HMPOs (where it is strongly heated) can be used as a useful probe of temperatures, densities, and luminosities, using simple isothermal clump models, even if each component (envelope, disk, jet, or cavity wall) is not resolved.

The objects chosen are near the centers of large scale massive molecular outflows mapped by Beuther et al. (2002b). IRAS 20343+4129 also has a compact high velocity outflow in

CO(2-1) centered on IRS1 (Palau et al. 2005). All have been found to have near-ir emission from shocked H₂ (Davis et al. 2004; Kumar et al. 2002). Two of them (IRAS 18151-1208 and IRAS 20343+4129 IRS3) were observed to have 0.5 and 1.3 mJy 3.6 cm emission, respectively (Carral et al. 1999). We observed IRAS 20343+4129 IRS1 and IRS3 with TEXES on Gemini North based on the 3.6 cm and H₂ observations, with the goal of studying the role of ionized gas in them.

The 10 μm grism spectral shapes of the HMPOs fall in three classes: those with deep silicate absorption; those with weak silicate absorption and an apparent peak at about 8 μm ; and those that rise monotonically from short to long wavelengths without an apparent silicate absorption feature. Since the HMPOs were chosen to have IRAS colors similar to UC HII regions (Sridharan et al. 2002) one would expect the HMPOs to have similar 10 μm spectra, and examples of these shapes can be seen in the UC HII spectra presented by Faison et al. (1998). Two of the ten HMPO grism spectra show strong [NeII] lines, IRAS 18247-1147 and 18530+0215. Sridharan et al. (2002) reported relatively strong 3.6 cm fluxes of 47 and 311 mJy, respectively, for them. We did not observe them with TEXES on Gemini in order to focus on the earliest possible HMPO stage associated with ionized gas. One of our objects, IRAS 20343+4129, was observed with the IRAS LRS and has a silicate absorption feature (Volk et al. 1991). The three objects presented here include an example of each of the three classes of grism spectral shapes.

Deriving physical information from the continuum spectra is difficult because the actual geometry of the dust is unknown, except that the sizes of the N band and 24.8 μm images limit the extent of the emitting structures. Experience with one-dimensional radiative transfer models of spectral energy distributions from UC HII regions (Campbell et al. 1995, 2000, 2004), and inspection of the new spectra themselves suggest that there are ranges of temperatures in the emitting regions. However, the two-dimensional radiative transfer models of Whitney et al. (2003a,b, 2004) show that the orientation of the outflow cavities dramatically affects the depth of the silicate absorption feature, as does emission and absorption by individual clumps in a clumpy dust cloud in the three-dimensional models of Indebetrouw et al. (2006). The recent observations of De Buizer & Minier (2005) and De Buizer (2006) of dust on outflow cavity walls also indicate that one-dimensional models are unrealistic. A simple approach that will allow us to derive approximate temperatures, column densities, and masses of different dust components is to assume a three-component model for the mid-ir continuum emission. The components are (1) a hot component whose size is constrained by the N band image, (2) a cool component whose size is constrained by the 24.8 μm image, and (3) a cold, pure extinction component that is responsible for the silicate feature. The first component could be a relatively compact disk, or a clump very near the HMPO. The second component could be a more extended (part of a) disk, or a clump of dust further out,

perhaps on the inner wall of one of the outflow cavities that would be expected to be present. The important point is that the amount of matter near the HMPO can be approximately determined.

Deriving information from the ionic lines is in principle straight-forward. The line fluxes can be corrected for local extinction based on the continuum models discussed above, and then the ratio of [NeII] to [SIV] fluxes can be used to determine the stars excitation temperature (Lacy et al. 1982; Okamoto et al. 2001). The excitation temperature can then be compared to that of a star deduced from the cm continuum flux. In addition, comparison of Doppler velocities of the ionic lines to those of molecular lines can be used to indicate if the gas is in an UC HII region or a jet.

2. Observations and Reduction

2.1. MIRSI Images on the IRTF

MIRSI, the Mid-InfraRed Spectrometer and Imager (Deutsch et al. 2002), was operated remotely from Colby College and The Center for Astrophysics on the IRTF for these observations. MIRSI has an imaging field of view of $85 \times 65''$ on the IRTF, with diffraction limited performance ($0.8''$ at $10\mu\text{m}$, and a plate scale of $0.2666''/\text{pixel}$). The objects presented here were imaged on 2003 September 13. From a trial observation of HMPOs during a 2002 engineering run, we expected the sources to be unresolved or marginally resolved. Conventional chopping and nodding was used with chopper throw $25''$ NS and telescope nod $25''$ EW, so that all chop-nod images were on the array. Five dithered 12 second integrations were taken through an N band filter and through a 7.9% wide filter centered at $24.8 \mu\text{m}$ of the IRAS 18151-1208 and IRAS 20343+4129 fields. Both IRAS 20343+4129 IRS1 and IRS3 were present in the latter field.

Excess electronic pattern noise was removed with a custom IDL procedure (Kassis et al. 2003). Chop-nod addition and subtraction and flat fielding were done in the usual way. Negative chop-nod images were inverted, and all individual images from the dithered chop-nod sets were combined in IRAF.

Positions were determined relative to those of the calibration stars without special care for precision astrometry, so the positions are limited by the inherent offsetting accuracy and stability of the IRTF on that night to several arcseconds. Since IRAS 20343+4129 IRS1 and IRS3 were observed simultaneously in each individual frame, their offset is quite accurate, and the identification of the mid-ir sources with the K band sources (Kumar et al. 2002) is quite certain, although it is not known if the mid-ir centers fall exactly on the K band

centers. We assume that IRAS that IRAS 18151-1208 is coincident with the peak of 3.6 cm emission (Carral et al. 1999). Positions are shown in Table 1 for the sources.

Simple photometry was performed using the IRAF task imexamine. The K stars γ Aql and γ Dra were used for point spread functions (PSFs) and photometric flux density calibrations. N band magnitudes for calibration were taken from the list of bright infrared standard stars on the IRTF web site. We used N band effective wavelengths and flux densities for zero magnitude as given by Tokunaga (2000). For the MIRSI 24.8 μm filter, we used a zero mag flux density calculated the formula given by Engelke (1992) shifted to agree with the N band zero mag flux density given by Tokunaga (2000). We assumed that the 24.8 μm magnitude would equal the Q mag (Cohen, et al.(1995)). This procedure gave agreement with the IRAS color corrected 25 μm flux density of 27.0 Jy for γ Dra within 1%. We did not determine extinction coefficients, and used the mean values for N and Q given by Krisciunas et al. (1987). The sky conditions varied during the night, making the systematic uncertainty in the flux densities large. There was a 30 % increase in raw flux for γ Aql in two adjacent dither sets of 5 second integrations through the 24.8 μm filter ($\pm 13\%$ variation from the mean of the two). In general, flux densities appear to be accurate to $\pm 10\%$, but the overall systematic accuracy is probably $\pm 30\%$. The flux densities are shown in Table 1, including the values used for γ Aql.

Images of IRAS 18151-1208 and 20343+4129 IRS1 appear to be unresolved at both wavelengths with indications of the first diffraction ring. IRAS 20343+4129 IRS3 is marginally resolved at both wavelength. FWHM values of Gaussians fit to the profiles by IRAF are shown in Table 1. Our observations and "pipeline" image processing for the HMPO survey were not intended for image deconvolution. We characterize the PSFs by values shown in Table 1 that are averages of Gaussian FWHM values and their standard deviations from calibration star observations over the course of the night. The standard deviation in the PSF could be due to small errors in shifting individual images before averaging and/or varying seeing in the unstable atmosphere.

An image of the IRAS 20343+4129 field at 24.8 μm are shown in Figure 1. The extended nature of IRS3 is clear in Figure 1.

2.2. MIRSI Grism Spectra on the IRTF

Grism spectra of the sources were obtained on 2003 September 14. The MIRSI grism was used with an N band prefilter, cutting off the spectra just longward of [NeII] 12.8 μm . The slit was oriented NS, and the system can be thought of as a long slit spectrometer. On

E. Tollestrup’s suggestion, we arranged both chop and nod to be NS so that four spectra were recorded in each 30 second integration camera frame.¹ We experienced considerable difficulty centering the source on the slit, and only one of the chop-nod images could be well centered on the slit at best. For each source, multiple 30 second integration frames were taken, although not all could be used.

The initial processing involved the following steps: (1) For each chop-nod subtracted camera frame, the electronic pattern noise was determined from the 20 column channel of the chip blanked by the N band filter’s long wavelength cutoff, and subtracted. (2) The frames were flat-field corrected using a dome flat from which a dark frame had been subtracted. (3) If necessary, excessively noisy pixels were zeroed. (4) All camera frames were averaged into a single combined frame with the IRAF task `combine`. (5) Copies of the combined frame were inverted and shifted as necessary, and then all four chop-nod spectra were averaged to a single combined spectrum using the `combine` task. (6) A bad pixel mask was applied to the single combined spectrum. (7) Based on inspection of the baseline surrounding the combined spectrum, a second pattern noise correction was performed if necessary using the region outside the spectrum. This processing proved capable of recovering spectra where there was no signal visible in raw data frames. IRAS 18151-1208 had strong signal visible, but both sources in 20343+4129 appeared only barely visible after the first stage of pattern noise correction, and IRS1 suffered from a noisy portion of its single usable frame.

For the sources here, μ Cep, an M supergiant, was used to calibrate the spectra. M supergiants are variable, and less desirable than the K giants used as photometric standards, but μ Cep gave an extremely high S/N calibration spectrum. The μ Cep grism spectra were processed in the same way as the HMPO spectra. In order to use our μ Cep, spectrum for flux calibration, we obtained ISO SWS spectra from the University of Calgary web site http://www.iras.ucalgary.ca/satellites/~volk/getswsspec_plot.html. This site uses a program to extract spectra as given by Sloan et al. (2003). Three spectra are available for μ Cep, and they show some minor differences. We chose TDT 05602852 for μ Cep because it appeared best based on inspection of separate up and down scans kindly provided by Kraemer (2006).

The IRAF task `apall` was used to extract the HMPO spectra and the μ Cep spectrum. A linear grism dispersion relation was created using the telluric lines near 10 μ m and the [NeII] 12.8 μ m line. The atmospheric transmission spectrum was taken from the UKIRT

¹MIRSI’s electronics adds multiple chip frames, in this case of 700 ms duration, recorded as extensions in fits files. Separate fits extensions are recorded for each chop and nod position, and are then appropriately added or subtracted to make up a camera frame. The nominal integration time would be the on-source time if the chopping and nodding were off the chip.

web site, convolved with the grism response, and cross-correlated to the uncalibrated MIRSI μ Cep spectrum to determine one wavelength-pixel point. The [NeII] 12.8 μm line was used with the IRAS 18247-1147 spectrum in which it was detected for the second point.

A custom IDL procedure was used to calibrate the HMPO spectra to the ISO μ Cep flux densities. However, we did not know how well the sources were centered on the slit, so a final step was made, following a suggestion by E. Tollestrup. For each preliminary calibration, the flux densities, F_λ , were summed over the spectrum, compared to the flux, F , as measured photometrically through the N band filter, and multiplied by a correction factor so that they would be the same. Flux densities in Janskys, F_ν , were calculated from F_λ for presentation in this paper. The calibrated spectra are shown in Figure 2. The 24.8 μm flux densities in Table 1 compared to the spectra indicate that the SEDs all rise significantly with increasing wavelength.

2.3. TEXES Spectra on the Genini N

3. Models of the Mid-IR Emission

3.1. Overview of a Simple Dust Continuum Model

As explained in the Introduction, the geometry of the mid-ir emitting dusty clouds is unknown except for constraints on their projected diameters. We can make simple three-component models to match our spectra and photometric data, and the models give estimates of the temperatures of the dust clumps, the column densities through them, the clump masses, and the mid-ir luminosities. Our models should *not* match the SEDs outside the mid-ir: we would expect them to underestimate the observed SED at both ends of the spectrum.

As stated in the Introduction, the components are (1) a hot component whose size is constrained by the N band image, (2) a warm component whose size is constrained by the 24.8 μm image, and (3) a cold, pure extinction component that is responsible for the silicate feature. In order to understand clearly the relationships of the various model inputs, we review the emission of an isothermal, constant density, dusty clump observed through a colder cloud that creates extinction but no emission. The observed flux density, F_λ , is given by

$$F_\lambda = \Omega B_\lambda(T)(1 - e^{-\tau_e(\lambda)})e^{-\tau_a(\lambda)} \quad (1)$$

where Ω is the solid angle of the clump, $B_\lambda(T)$ is the blackbody intensity, $\tau_e(\lambda)$ is the optical depth of the emitting clump, and $\tau_a(\lambda)$ is the extinction optical depth of the absorbing

(and scattering) overlying cloud. For an optically thin clump, the emissivity, $\epsilon(\lambda)$, is simply $\epsilon(\lambda) = \tau_e(\lambda)$. The optical depth in emission is given by

$$\tau_e(\lambda) = K_e(\lambda) \int_{Clump} \rho_d dl \quad (2)$$

where $K_e(\lambda)$ is the absorption cross section per mass of the emitting dust in cm^2g^{-1} , ρ_d is the mass density of the dust, and the integral is through the emitting clump. The integral through the clump can be related to the column density of H nucleons, N_H through

$$\int_{Clump} \rho_d dl = \frac{M_d}{M_g} \mu m_H N_H \quad (3)$$

where $\frac{M_d}{M_g}$ is the dust to gas mass ratio, μ is the mean molecular weight for the assumed abundance ratios, assuming neutral atomic gas in order to use the column density of H nucleons (as opposed to H_2), and m_H is the mass of a hydrogen atom. Thus the emission optical depth can be related to the column density:

$$\tau_e(\lambda) = K_e(\lambda) \frac{M_d}{M_g} \mu m_H N_H \quad (4)$$

We can now clearly see from equation (1) that the observed flux density, F_λ is related to both the solid angle and the column density, and that the derived column density is strongly dependent on the assumed solid angle. For the simple geometry of an end-on cylindrical cloud whose solid angle is estimated from the observed angle, θ_{FWHM} , $\Omega = \frac{\pi}{4} \theta_{FWHM}^2$, and in the optically thin case

$$F_\lambda = \frac{\pi}{4} \theta_{FWHM}^2 B_\lambda(T) K_e(\lambda) \frac{M_d}{M_g} \mu m_H N_H e^{-\tau_e(\lambda)} \quad (5)$$

The assumed projected diameter of the clump is thus clearly a key factor in deriving a reasonable column density. For optically thick clouds, the exponential function in the expression for emissivity $\epsilon(\lambda) = (1 - e^{-\tau_e(\lambda)})$ makes the column density estimate very strongly dependent on the assumed diameter.

Estimating the source diameter is straightforward for marginally resolved sources like IRAS 20343+4129 IRS3 (see Table 1), if we assume that the profiles of the true source, the observed data, and the PSF are all Gaussians. With that assumption, a formal deconvolution would give

$$\theta_s = \sqrt{\theta_d^2 - \theta_p^2} \quad (6)$$

where θ_s is the true source FWHM, θ_d is the observed data FWHM, and θ_p is the PSF FWHM. Let us represent θ_d in terms of θ_p and n standard deviations of the PSF FWHM, σ_p : $\theta_d = \theta_p + n\sigma_p$. Substituting this expression into Eq(6) gives

$$\theta_s = \sqrt{2n\sigma_p\theta_p + n^2\sigma_p^2} \quad (7)$$

An observation of a source with a true value of θ_s in which the statistical variation resulted in a $-n\sigma - p$ deviation from $\theta_d = \theta_p + n\sigma_p$ would appear to be unresolved with observed, $\theta_d = \theta_p$. Thus we can estimate reasonably likely values for source size θ_s from a 1σ deviation by substituting $n = 1$ into Eq (7), and a 3σ upper limit to a source size by substituting $n = 3$. The resulting values of θ_s are larger than σ_p or $3\sigma_p$ because of the deconvolution. Table 2 presents diameters for the hot components and the warm components calculated from the Gaussian FWHM values in Table 1 in N band and at $24.8 \mu\text{m}$, respectively. They have been converted to AU at the distances of the HMPOs for the table.

The derived column densities depend on the dust model that specifies $K(\lambda)$. A very attractive model is that of Ossenkopf & Henning (1994) for protostellar cores often referred to as OH5. This dust represents coagulated grains with ice mantles that would be expected to form from dust originally in the diffuse interstellar medium during the process of molecular cloud formation. It has been used to fit submm SEDs of high-mass protostellar cores (van der Tak et al. 1999, 2000) and far-ir observations of the UC HII region G34.3+0.2 (Campbell et al. 2004). However, when we examined its $K(\lambda)$ behavior around $10 \mu\text{m}$, we found that its silicate feature is shifted longward from $9.7 \mu\text{m}$ and broadened so that it does not appear to be compatible with our grism spectra. Consequently we are using a dust model for the diffuse interstellar medium that appears to fit better the shape of our observed silicate absorption feature. We have chosen the 2003 synthetic extinction curve of Draine (2003a) and colleagues for Milky Way, R=3.1 dust that is available on his web site. Although it was not developed for molecular cores, this model is accessible, well known, and well documented.

The shape of the grism spectrum of IRAS 18151-1208 (Fig. 2) together with the large flux density at $24.8 \mu\text{m}$ (Table 1), requires a minimum of three components for our models: hot dust responsible for the $8 \mu\text{m}$ end of the grism spectrum, warm dust for the $13 \mu\text{m}$ end of the spectrum and the $24.8 \mu\text{m}$ photometry, and cold dust for the depth of the silicate absorption. The model calculation has the following input parameters: the temperature of the hot component, T_h , the diameter of the hot component θ_h , the optical depth in emission of the hot component at $9.70 \mu\text{m}$, τ_h , the analogous parameters for the warm component, T_w , θ_w , and τ_w , and the extinction optical depth, τ_a , of the overlying cloud that is too cold to emit in the mid-ir. In the mid-ir, the extinction is virtually pure absorption. The model predicts a spectrum to match the observations that is the sum of the contributions of both hot and warm components according to Eq(1). For given optical depths, column densities,

N_H , can be derived from Eq(4) for each component, using parameters found in Draine’s web site for the dust model. For end-on cylindrical geometry, the mass of the hot and warm components can be derived from N_H . Visual extinctions are calculated from $\frac{A_V}{\tau_{9.7\mu m}} = 18.5$, as recommended by Draine (2003b). The SED due to the two dust clumps and overlying extinction can be calculated to verify that it does not create excessive emission outside the mid-ir, and to derive the luminosity of the mid-ir emitting clumps for comparison to measurements and estimates of the overall HMPO luminosity.

3.2. Fitting the Continuum Data

Our goal is apply our simple three-component model to the grism and 24.8 μm photometric data to derive reasonable estimates of the temperatures, the column densities, the masses, and luminosities of the emitting dust components, and the column density of the cold extinction component. We have no measurements of the angular extents of the components for IRAS 18151-1208 or 20343+4129 IRS1 because they were unresolved, although we do have them for 20343+4129 IRS3. If we assume incorrectly small sizes for the first two, we will make unrealistic over-estimates of the column densities. We have chosen to use large size estimates that are consistent with the data for these two so that our column densities can be thought of as less than or on the order of the true values. The parameters for our model are shown in Table 3. It uses the sizes based on 1 σ deviation estimates for unresolved sources in Table 2.

The best-fit temperatures of the hot and warm components are in the ranges 315-1600K and 110-163K, respectively. It is useful to examine SEDs over a wide range of wavelengths in order to understand how the components combine to fit the data. As an example we show the individual components’ emission SEDs in Figure 3 for a model of IRAS 18151-1208. In addition, Figure 3 shows their sum, and their sum with the cold component’s extinction. The 455K hot component shows a strong 9.7 μm silicate feature, as expected. However the 136K warm component is sufficiently cool that the silicate feature convolved with the Planck spectrum that is rapidly rising to long wavelengths does not appear as a distinctive peak. The combined SED is quite different from the separate SEDs. A range of temperatures would smooth out the structure in the SED in the mid-ir, of course. The cold absorbing layer’s 9.7 and 18 μm features are clear in the total spectrum, and the latter causes a nearly flat portion between 15 and 20 μm . The total SED also clearly shows that these components emit very weakly at both near-ir and submm wavelengths. Figure 4 shows how the model components compare to the grism and 24.8 μm data, and how the total model with absorption fits it. For IRAS 18151-1208, a large range in T_h will fit the data, apparently because the the entire

grism spectral range lies in the Raleigh-Jeans part of the hot component’s spectrum. We have presented a model with a low value of T_h here. Its parameters are shown in Table 3. We also present in Table 3 a model with $T_h = 1600K$, a commonly assumed dust sublimation temperature (Whitney et al. 2004).

The models were interactively fit to the data. In order to quantify the quality of the fit and to aid in choice of extreme values of the parameters consistent with the systematic accuracy of the data, we defined a modified χ^2 statistic. The grism was broken into four photometric bands: $8.0 - 9.0\mu\text{m}$, $9.0 - 10.5\mu\text{m}$, $10.5 - 12.0\mu\text{m}$, and $12.0 - 13.0\mu\text{m}$. Fluxes were summed in each band. The $24.8\mu\text{m}$ photometry was a fifth band. We defined the modified χ^2 statistic for each band, i , as

$$\chi_{mi}^2 = \frac{(F_{i,Model} - F_{i,Data})^2}{F_{i,Data}^2}$$

where F_i is the flux in band i . The sum of the five terms formed χ_m^2 for the model. This statistic places the quality of the fit as a fraction of the data value in each band on equal footing. Even though it assumes that each of the five bands has equal S/N and has no specific statistical interpretation, it is useful for fitting models to the data. For optimizing models, we sought to minimize χ_m^2 . For choosing the upper or lower value of a specific parameter (e.g. T_w) that might be reasonable, we started with the value in an optimum model, and varied the parameter until the band most affected by the parameter (in this case $i = 5$, $24.8\mu\text{m}$) indicated a 30% difference (our systematic photometric accuracy), or $\chi_{mi}^2 = 0.09$. On a graph of the data like Figure 4, the upper value T_w would cause the model’s point point to fall on the end of the upper error bar. Using a 30% difference between model and data is conservative: our procedure should not result in an artificially restricted range in extreme values. It was not feasible to vary more than one parameter at a time because of the size of the parameter space and the fact that all bands of our data were somewhat affected by all of the parameters.

3.3. General Results of the Continuum Models

Parameters for the models are presented in Table 3. Two models are given for IRAS 18151-1208 (hereafter 18151) at extreme ends of the range of T_h that fits the data well, and the best-fit model is given for each of IRAS 20343+4129 IRS1 and IRS3 (hereafter 20343 IRS1 and 20343 IRS3). In addition, upper and lower extreme values that are consistent with the data to within 30% as discussed above are shown.

There are a number of very striking aspects of the values derived from the models. The

first is that the source that appears most deeply embedded, 18151, has a hot component temperature that is sufficiently high that its mid-ir is on the Rayleigh-Jeans end of the spectrum, so that the temperature cannot be determined without measurements in shorter bands like L or M. For the other two objects, Table 3 shows moderate ranges in temperatures from lower to upper values. The ranges in T_h and T_w are well separated in all of the sources. If each source’s emission is from a single clump or disk with a continuous range in temperatures, each must contain a wide range in the actual temperatures.

It is interesting to note that the temperatures for what we call warm dust, T_w , are rather close to those of the “hot component” of Sridharan et al. (2002) based on IRAS data (T_{hd} , of 170 K and 150 K for 18151 and 20343, respectively). It suggests that our IRTF measurements are measuring much of the same dust as the shorter IRAS bands measured. In fact, our N band F_ν values for 18151 and 20343 IRS1 + IRS3 are each slightly more than 50% or the IRAS PSC values. Our 24.8 μm F_ν for 18151 virtually equals the IRAS PSC 25 μm value, and the sum of the 20343 F_ν values is 2/3 of the IRAS value.

Another interesting aspect is the extremely small amount of gas and dust in the hot component. This material is unlikely to be a massive accretion disk that might be expected for an HMPO. Although the assumed diameters of the hot components are somewhat arbitrary and affect $N_{H,h}$, they do not affect the mass estimates since these components are optically thin. The ranges about the central value of $N_{H,h}$ and M_h are about $\pm 30\%$, as expected for optically thin sources. Lower limits to $N_{H,h}$ based on the 3σ upper limits on source diameters shown in Table 2 can be calculated from the data in Table 3 since N_H is inversely proportional to Ω for optically thin sources. Accurate estimates of $N_{H,h}$ and number density $n_{H,h}$ of the hot components of 18151 and 20343 IRS1 will require higher resolution observations on a larger telescope.

The optical depths in emission of the warm components, τ_w , are quite high, and are optically thick in the case of 18151. This effect is a surprise because the assumed value of D_w is not small in relationship to observed and expected diameters for structures near HMPOs (De Buizer & Minier 2005; Shepherd et al. 2001). For 18151, the mass and $N_{H,w}$ are not accurately determined because of the high optical depth, and an upper value could not be determined. The indicated $N_{H,w}$ is larger than the column density for extinction, $N_{H,a}$. Even with these high values, however, the masses are less than $1 M_\odot$ and much less than the mass expected for the HMPO. This situation suggests that the warm dust is not part of a high mass accretion disk during a period of rapid accretion. For 20343 IRS1 and IRS3, τ_w is nearly optically thick. Since IRS3 was resolved, the values for $N_{h,w}$ and mass are good estimates and show rather high $N_{h,w}$ even though the mass is only $0.019 M_\odot$.

Extinction optical depths, τ_a , are relatively small, and cover a limited range. There

is a selection effect: if they were larger, we would not have detected the HMPOs in the mid-ir. The appearance of the 20343 IRS3 grism spectrum suggested that there might not be any extinction, but fitting the spectrum required all of the components. The range in τ_a from lower to upper value is small because the extinction is exponential and the sources are optically thick in extinction. The values of $N_{H,a}$ and A_V are also relatively small since they are directly proportional to τ_a . Unlike the emitting components, the extinction τ_a and parameters derived from it ($N_{H,a}$ and A_V) are not affected the assumed source size, and hence are more firmly defined values.

Comparison to the values for N_{gas} and A_V from 1.2 mm observations given by Beuther et al. (2002a) would indicate how deeply embedded each HMPO is within the larger dust clump mapped at 1.2 mm if the clumps were not themselves clumpy on the scale of the IRTF observations. If the HMPO were at the center of one of the Beuther et al. (2002a) clumps, we would expect mid-ir based values to be one-half the 1.2 mm-based values, after appropriate compensation for the different dust models used here and by Beuther et al. (2002a). Beuther et al. (2005) recommend that values for 1.2 mm-based N_{gas} and A_V from Beuther et al. (2002a) should be reduced by a factor of 2. We have used column density of H nucleons with the Draine (2003a) dust model, whereas N_{gas} is based on H₂. Draine (2003a) also used a gas:dust mass ratio of 124 versus 100 (Beuther et al. 2002a). The value of the absorption cross section per mass $K_e(1.2mm)$ we used is $0.217 \text{ cm}^2 g^{-1}$ compared to $0.407 \text{ cm}^2 g^{-1}$ that would be used by Beuther et al. (2005). The result is that our values for N_H would be 2.34 larger than those of Beuther et al. (2005). Since the conversion from N_{gas} to N_H is a multiplication by 2, and N_{gas} should be reduced by 2, simply multiplying N_{gas} from Beuther et al. (2002a) by 2.34 gives N_H based on Draine’s dust model used here. Our ratio of $\frac{A_V}{N_H}$ also differs that of Beuther et al. (2002a) and Beuther et al. (2005). The values of A_V given by Beuther et al. (2002a) can be multiplied by 1.59 to be consistent with a reduction of 2 (Beuther et al. 2005) and conversion to our model using Draine (2003a) dust modified by $\frac{A_V}{\tau_{9.7\mu m}} = 18.5$. The $N_{H,a}$ and A_V of 18151 component 1 of Beuther et al. (2002a) are 8.0 times larger than our values after conversion to our dust assumptions. Values for 20343 component 1 (Beuther et al. 2002a) are 6.6 times large than our values for 20343 IRS1. For 20343 IRS3 the ratio is 20. If the 1.2 mm clumps, are not themselves clumpy, the mid-ir HMPOs cannot be at the centers based on $N_{H,a}$ and A_V . The mid-ir HMPOs could only be near the centers of the overall clumps if the clumps are clumpy and the mid-ir is observed through gaps. There are also offsets in the plane of the sky between the apparent mid-ir positions and the 1.2 mm peaks, so the differences in $N_{H,a}$ and A_V are not surprising.

Subject to the limitations of our assumptions, our models can be used to estimate the HMPOs’ luminosities rather well. If the observed mid-ir comes from circumstellar dust that absorbs and reradiates most of the HMPO’s emission, then the luminosity calculated from

the hot and warm components is an accurate estimate. In Table 3, we show the luminosity as observed through the extinction, $\frac{L_o}{L_\odot}$, for comparison to other mid-ir luminosity estimates that do not account for local extinction. We also show the luminosity emitted by the hot and warm clouds without the extinction factor, $\frac{L_e}{L_\odot}$ as our estimate for the total luminosity. If the cold extinction layer in our model re-radiates in the far-ir, an observed full SED should have the same luminosity, $\frac{L_e}{L_\odot}$. If we have observed the dominate HMPOs for each region, our values should be close to luminosities based on IRAS presented by Sridharan et al. (2002). For 18151, our estimate is 25,000 L_\odot in close agreement to the IRAS based value of 20,000 L_\odot (Sridharan et al. 2002). For 20343 IRS1 and IRS3 combined, our value is 1,450 L_\odot , about half of 3,160 L_\odot from IRAS. Overall, these agree well. Earlier we noted remarkably close agreement between our flux densities and those of the IRAS PSC, and between our T_w and the IRAS-based T_{hd} of Sridharan et al. (2002). Consequently the agreement of luminosities is to be expected.

4. Analysis of High Resolution Spectra

5. Discussion of Individual Sources

6. Conclusions

We are grateful to R. T. Brooks of Colby College for work on improving the grism spectra reduction process, and for Dr. John W. Kuehne of Colby for system administration of the workstations used for data acquisition, reduction, and modeling. Miranda Harwarden-Ogata and Eric Tollestrup provided tireless support from the IRTF for the remote observing program.

Facilities: IRTF, Gemini.

REFERENCES

- Beuther, H. et al., 2002a, ApJ,566,945
 Beuther, H. et al., 2002b, A&A, 383, 892
 Beuther, H. et al., 2005, ApJ,533, 535
 Beuther, H. et al., 2006, Planets and Protostars V, astro-ph/0602012

- Campbell, M. F., et al., 1995, ApJ, 454, 831
- Campbell, M. F., et al., 2000, ApJ, 536, 816
- Campbell, M. F., et al., 2004, ApJ, 600, 254
- Carral, P., et al., 1999, Rev. Mexicana Astron. Astrofis., 35, 97
- Cohen, M., et al., 1995, AJ, 110, 275
- Davis, C. J., et al., 2004, A&A, 425, 981
- De Buizer, J. M., & Minier, V. 2005, ApJ, 628, L151
- De Buizer, J. M. 2006, ApJ, 642, L57
- Deutsch, L. et al., 2002 in Astronomical Telescopes and Instrumentation, SPIE 4841, 106
- Draine, B., 2003a, <http://www.astro.princeton.edu/~draine/dust/dustmix.html>.
- Draine, B., 2003b, ARA&A, 41, 241
- Engelke, C. W., 1992, AJ, 104, 1248
- Faison, M., et al., 1998, ApJ, 500, 280
- Indebetrouw, R. et al., 2006, ApJ, 636, 362
- Kasis, M., et al., 2002, AJ, 124, 1636
- Kasis, M., 2003, private communication
- Kasis, M., et al., 2006, ApJ, 637, 823
- Krisciunas, K. et al., 1987, PASP, 99, 887
- Kraemer, K. E., 2006, private communication
- Kumar, M. S. N., et al., 2002, ApJ, 576, 313
- Lacy, J. H. et al, 1982, ApJ, 255, 510
- Lacy, J. H. et al, 2002, PASP, 114, 153
- Okamoto, Y. K., et al., 2001, ApJ, 553, 254
- Ossenkopf, V., & Henning, T., 1994, A&A, 291, 943

- Palau, A., et al., 2005, poster at Submillimeter Astronomy in the era of the SMA, Harvard University
- Shepherd, D. S. et al., 2001 *Science*, 292,1513
- Sloan, G. C., et al., 2003, *ApJS*, 147, 349
- Sridharan, T. K. et al., 2002, *ApJ*, 566, 931
- Tokunaga, A. T. , 2000 in *Allens Astrophysical Quantities*, 4th ed, A. N. Cox, ed, Springer: New York, p 150
- van der Tak, F. F. S., et al., 1999, *ApJ*, 522, 991
- van der Tak, F. F. S., et al., 2000, *ApJ*, 537, 283
- Volk, K., et al., 1991, *ApJS*, 77, 607
- Whitney, B. A., et al., 2003a, *ApJ*, 591, 1049
- Whitney, B. A., et al., 2003b, *ApJ*, 598, 1079
- Whitney, B. A., et al., 2004, *ApJ*, 617, 1177
- Zhu, Q-F., et al., 2005 *ApJ*, 631, 381

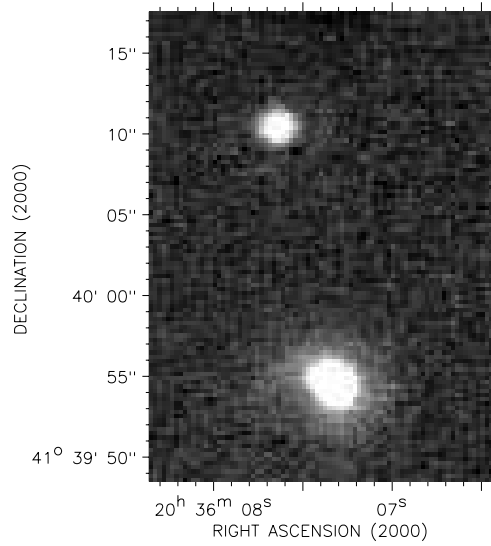


Fig. 1.— IRAS 20343+4129 at $24.8 \mu\text{m}$. IRS1 is in the NE, and IRS3 in the SW. There is less contrast in the appearance of the sources in N band, as would be expected from the more nearly equal brightnesses in N (see Table 1). The coordinates are taken from N band image. The true source positions are most likely to be at the K band positions of IRS1: $20^{\text{h}}36^{\text{m}}7.6^{\text{s}}$, $41^{\circ}40'8''.0$ (J2000) IRS3: $20^{\text{h}}36^{\text{m}}7.3^{\text{s}}$, $41^{\circ}39'52''.5$ (J2000)(Kumar et al. 2002). The 3.6 cm source of Carral et al. (1999) is within an arcsecond of IRS3.

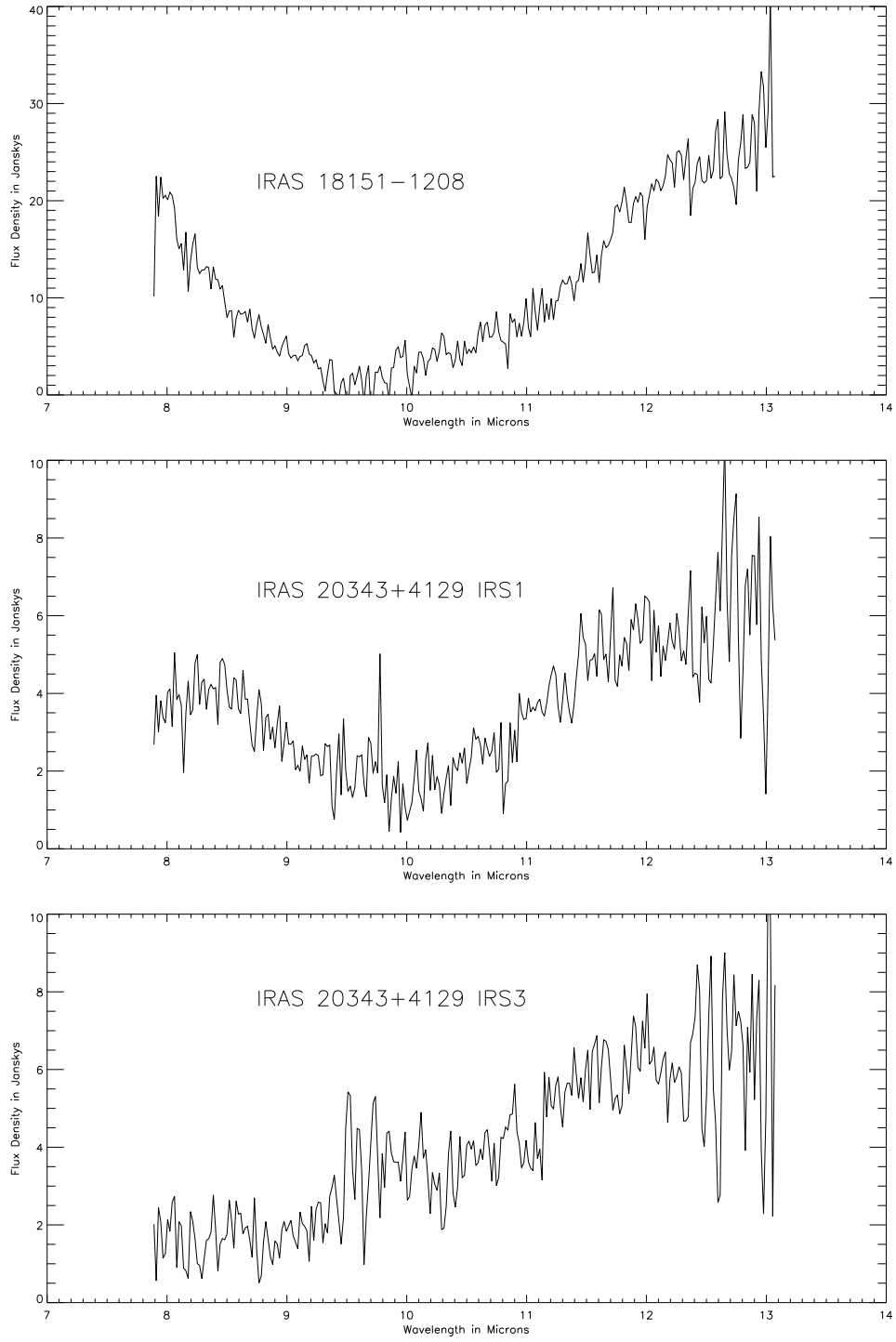


Fig. 2.— Grism spectra of the three sources.

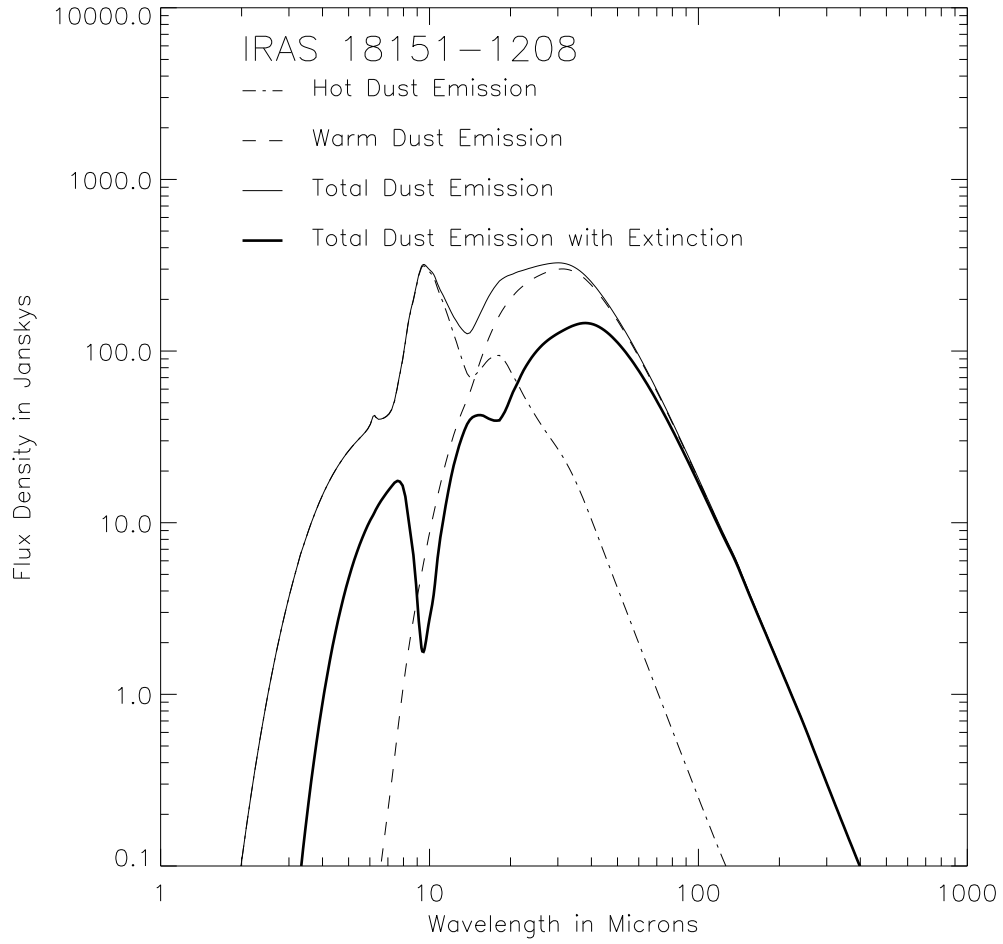


Fig. 3.— Individual and summed hot and warm components SEDs without extinction, and with extinction for IRAS 18151-1208. Parameters of the model are given in Table 3.

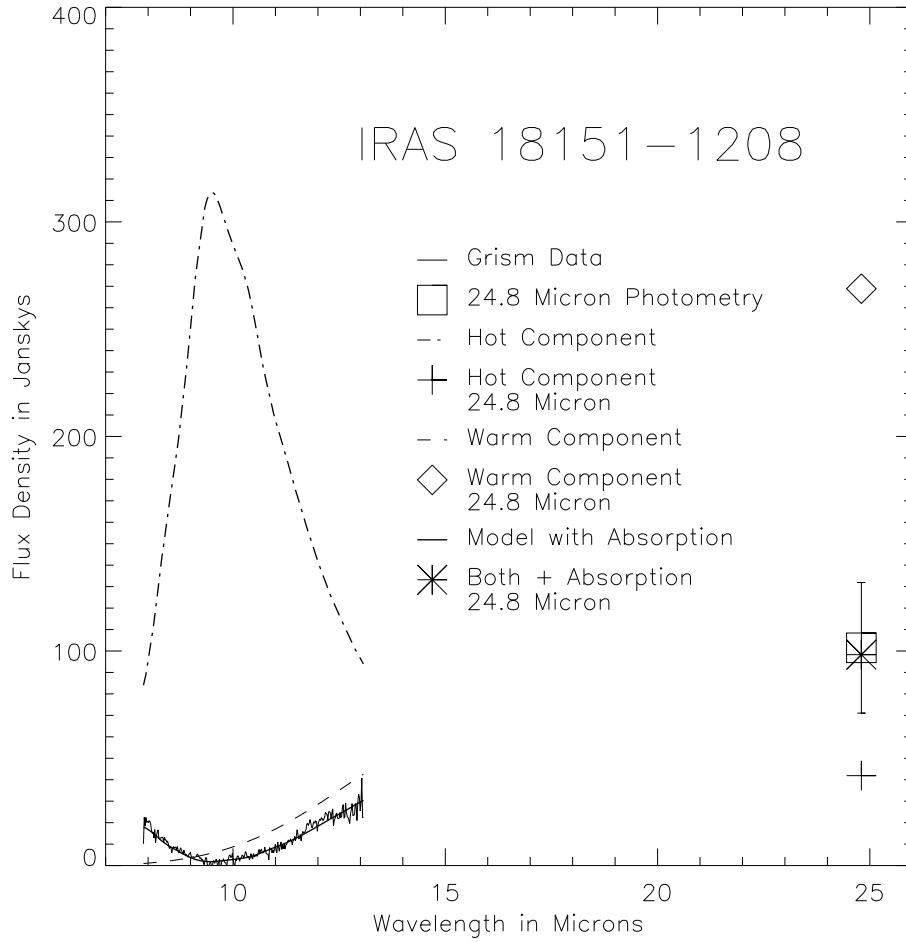


Fig. 4.— Individual and summed hot and warm components emission without extinction, and with extinction compared to the grism spectrum and 24.8 μm photometry for IRAS 18151-1208. Parameters of the model are given in Table 3.

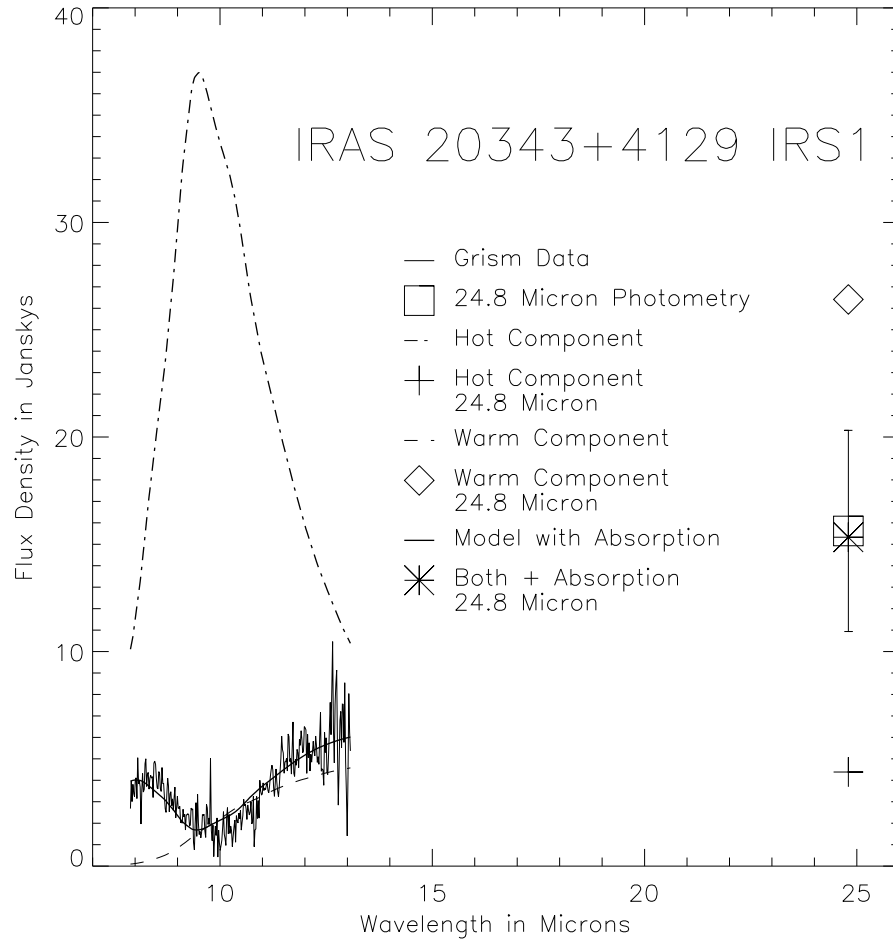


Fig. 5.— Same as Figure 4 for IRAS 20343+4129 IRS1.

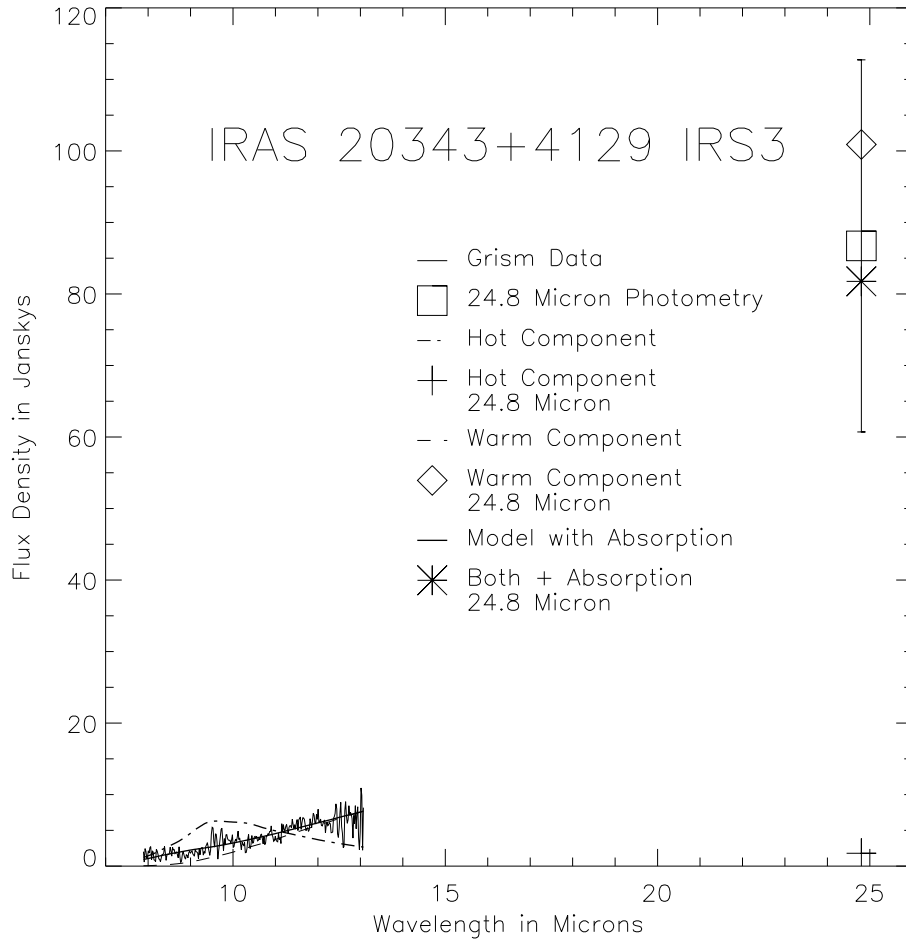


Fig. 6.— Same as Figure 4 for IRAS 20343+4129 IRS3.

Table 1. Image Data

Object	RA(2000)	DEC(2000)	$F_{\nu}(N)$ ¹	$F_{\nu}(24.8 \mu m)$ ¹	FWHM(N) ²	FWHM(24.8 μm) ²
IRAS 18151-1208	18:17:58.1 ^{3 4}	-12:07:25.6 ^{3 4}	11.2	101.4	1''01	1''91
IRAS 20343+4129 IRS1	20:36:7.6 ^{5 6}	41:40:08.0 ^{5 6}	8.1	15.6	0''91	1''88
IRAS 20343+4129 IRS3	20:36:7.3 ^{5 7}	41:39:52.5 ^{5 7}	3.7	86.6	1''24	2''41
γ Aql	19:46:15.6	10:36:47.7	72.2	13.6
PSF Average ⁸	0''99	1''83
PSF Standard Deviation	0''088	0''124

¹Janskys. Systematic uncertainty is $\pm 30\%$

²FWHM of Gaussian fit to image by IRAF task imexamine

³3.6 cm source position (Carral et al. 1999)

⁴IRTF indicated N position: 18:17:57.9 -12:07:27.0

⁵K source position (Kumar et al. 2002)

⁶IRTF indicated N position: 20:36:07.6 41:40:10.0

⁷IRTF indicated N position: 20:36:07.3 41:39:54.0

⁸Based on 6 observations in N and 5 at 24.8 μm

Table 2. Source Diameters for Models

Object	Distance, pc ¹	Hot Component, AU	Warm Component, AU	Assumption for Calculation
IRAS 18151-1208	3000	1280	2050	1 σ deviation for unresolved source ²
IRAS 18151-1208	3000	2310	3670	3 σ upper limit for unresolved source ²
IRAS 20343+4129 IRS1	1400	600	960	1 σ deviation for unresolved source
IRAS 20343+4129 IRS1	1400	1080	1720	3 σ upper limit for unresolved source
IRAS 20343+4129 IRS3	1400	1050	2200	Gaussian deconvolution of resolved source ²
IRAS 20343+4129 IRS3	1400	1590	2930	3 σ upper limit for resolved source

¹Sridharan et al. (2002)

²See text for details

Table 3. Source Model Parameters

Object	D_h^1 AU	T_h K	τ_h	$\log N_{H,h}$	$\log \frac{M_h}{M_\odot}$	D_w^2 AU	T_w K	τ_w	$\log N_{H,w}$	$\log \frac{M_w}{M_\odot}$	τ_a^3	$\log N_{H,a}$	$A_{V,a}$	$\log \frac{L_o}{L_\odot}^4$	$\log \frac{L_e}{L_\odot}^5$	χ_m^2
18151	1280.	455.	0.0540	21.14	-3.35	2050.	136.	8.00	23.31	-0.77	5.00	23.10	92.5	3.73	4.40	0.011
18151	1280.	1600.	0.0025	19.81	-4.69	2050.	163.	2.64	22.83	-1.26	4.90	23.10	90.7	3.85	5.35	0.014
20343 IRS1	600.	484.	0.0050	20.10	-5.05	960.	133.	0.41	22.02	-2.72	3.03	22.89	56.1	2.29	2.79	0.011
20343 IRS3	1050.	315.	0.0015	19.59	-5.07	2200.	110.	0.78	22.30	-1.72	0.99	22.40	18.3	2.81	2.92	0.016
Upper Values																
18151	1280.	1600.	0.0740	21.27	-3.22	2050.	171.	$\tau \gg 1$	INDEF ⁶	INDEF ⁷	5.33	23.13	98.7	3.91	5.35	NA ⁸
20343 IRS1	600.	523.	0.0064	20.21	-4.94	960.	144.	0.58	22.17	-2.57	3.45	22.94	63.9	2.37	2.86	NA
20343 IRS3	1050.	333.	0.0020	19.71	-4.95	2200.	113.	1.03	22.42	-1.60	1.35	22.53	24.9	2.91	3.01	NA
Lower Values																
18151	1280.	425.	0.0017	19.65	-4.85	2050.	124.	1.64	22.62	-1.46	4.55	23.06	84.2	3.64	4.33	NA ⁸
20343 IRS1	600.	450.	0.0038	19.99	-5.17	960.	122.	0.27	21.83	-2.91	2.79	22.85	51.6	2.21	2.71	NA
20343 IRS3	1050.	294.	0.0010	19.42	-5.25	2200.	104.	0.56	22.16	-1.86	0.68	22.24	12.6	2.69	2.80	NA

¹ Assumed diameter of hot component.

² Assumed diameter of warm component.

³ Optical depth of cold extinction component.

⁴ Luminosity "observed" due to hot and warm dust components with extinction of cold component applied.

⁵ Luminosity emitted by hot and warm dust components without application of extinction of cold component.

⁶ Source is optically very thick, so N_H cannot be determined.

⁷ Source is optically very thick, so mass cannot be determined.

⁸ Values are derived from multiple models for which the parameter's upper value shown gives $\chi_{m,i}^2 \simeq 0.09$ for the wavelength range most sensitive to the parameter.